

CONDUCTION IN THE TRANSITION REGION ? : INTERPRETATION OF DEMS USING SOHO/SUMER OBSERVATIONS

Scott W. McIntosh

ESA Research and Scientific Support Department, NASA/GSFC, Mailcode 682.3, Greenbelt, MD 20771. USA

ABSTRACT

The role of classical heat conduction in the energy balance of the T_e domain of the transition region ($10^5 - 10^6$ K) is explored. We consider variations in space and time of the Differential Emission Measure (DEM) inferred from high cadence (10s) SUMER observations taken on May 17, 1998 as part of JOP72. In particular, we show that the gradient of the DEM in the observed region, irrespective of the spatial/temporal binning applied, is $3/2$. We discuss the implications of this result.

1. INTRODUCTION

The exact form of the energy equation in the solar Transition Region (TR) is a topic of hot debate (see, e.g., Athay 1966; Jordan 1980; Craig et al. 1978; Rosner et al. 1978; Cally 1990; Mariska 1992). Details of the spatial and temporal inter-play, and relative strength, of the radiative, conductive and mechanical components of the equation in the TR remain illusive. The derivation of these energy fluxes relies heavily upon the acquisition of plasma diagnostic distributions, such as the Differential Emission Measure in temperature ($\text{DEM}(t_e) \equiv \xi(t_e)^1$), from remotely sensed UV/EUV emission line spectra; like those obtained by the Coronal Diagnostic Spectrometer (CDS; Harrison et al. 1995) and Solar Measurement of Emitted Radiation (SUMER; Wilhelm et al. 1995) on SoHO (Fleck et al. 1995).

In this paper we present some preliminary results from a run of SoHO JOP72 from May 17, 1998 (13:00-17:00 UT); further, more detailed analysis, will be found in McIntosh & Judge (2002; in preparation). This dataset encompasses high temporal, spatial and spectral resolution measurements, from SoHO (SUMER, MDI) and the Transition Region and Coronal Explorer (TRACE; Handy et al. 1999); For details of this observing program see Judge et al. (2001) and Fig. 1 of this paper for a context image of the SUMER observations.

This paper is laid out as follows: In Sect. 2 we will briefly discuss the data, its reduction and the steps

followed that allow us to compute a discretized $\xi(t_e)$ at each spatial pixel and timestep over the duration of the observations, effectively creating a map, $\xi(t_e, x, t)$. In Sect. 3 we show the two principal components of such maps; namely, the gradient of the DEM, $\beta (\equiv d(\log_{10} \xi)/dt_e)$, and the “absolute” value of the DEM, $\xi_0 (\equiv \log_{10} \xi(t_e = 5))$, in the temperature region spanning the classical TR, ($5 \leq t_e \leq 6$). We also discuss the temporal and spatial averaging of these maps to construct distributions of β and ξ_0 and suggest how they contribute to the energy balance of the TR. In Sect. 4 we will discuss the further application of the material presented herein that will be published in a future article.

2. SUMER DATA & DEM(T_E, X, T) ANALYSIS

Our primary concern in this paper is the use of the observed SUMER data to compute a map of the spatial and temporal variations in the DEM, $\xi(t_e)$, over the perceived TR temperature interval ($5 \leq t_e \leq 6$). These maps can then be used as a construct to study the energy balance of the TR in a similar manner to Jordan (1980).

The full resolution SUMER data (1”x120”; slit #5) has a ten second exposure and has five spectral windows, each fifty spectral pixels wide. Some details of the spectral windows/lines observed can be found in Table 1. Reducing the data follows the usual pattern of concatenation, flat-fielding, geometric, dead-time, local-gain, and finally, the radiometric corrections². The total number of photons to hit the detector over the course of the time-series is $3.e6$, some order of magnitude down on the $1.e7$ required to perform a dead-time correction on this particular dataset. However, it is necessary that the local-gain correction to be applied for pixels at the top of the slit.

As stated above, we are interested in the derivation of $\xi(t_e)$ at each spatial pixel and for each time step. Unfortunately, we have reduced signal-to-noise in the lower “quiet” part of the slit (positions ≥ 50) for the cooler lines and so we will focus on the upper “plage” region of the slit (positions < 50) for our analysis to ensure that the temperature coverage is as

¹Throughout we will use t_e to denote the base-10 logarithm of the electron temperature, T_e .

²Further details of the reduction process can be found in McIntosh & Judge (2002).

Table 1. Details of the SUMER JOP 72 data acquired on May 17, 1998. We provide, the wavelength and the temperature of the line's emissivity maximum $\tau (= \log_{10} T_e^*)$.

Ion	λ (Å)	τ
N III	764.350	5.00
N IV	765.143	5.12
O IV	787.710	5.16
O V	760.228	5.34
Ne VIII	770.400	5.76
Ne VIII	780.324	5.76

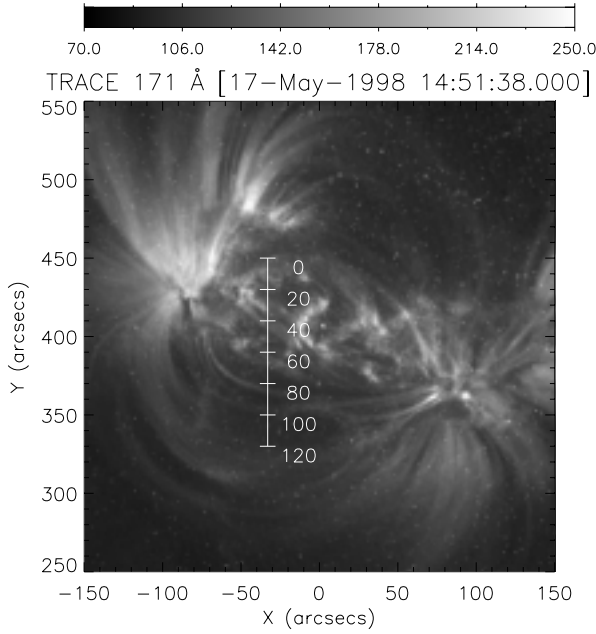


Figure 1. Context for the 17 May, 1998 “pm” time-series (see Judge et al. 2001, for details). This shows the position of the SUMER slit superimposed on the TRACE 171 Å image taken just prior to the start of the time-series. Clearly, the slit spans regions of active and quiet solar plasma.

uniform as possible; to omit the cooler lines severely impedes the following analysis. Figure 2 provides a graphical depiction of the temperature dependence of the observed emission lines and $\xi(t_e)$ used in this analysis.

Of course, there are core assumptions required to compute the $\xi(t_e)$ from the observed line intensities (see, e.g., Mason & Monsignori-Fossi 1994), but for the sake of brevity we will not re-iterate those here. However, it is important to note that we are assuming a time-independent ionization balance and that each exposure observes an equilibrium “snap shot” of the TR plasma; some *very* restrictive assumptions. Thus, we compute the $\xi(t_e)$ on a *six* point grid spanning the $t_e = [5, 6]$ region, as demonstrated by the points on the upper panel of Fig. 2. such that, for

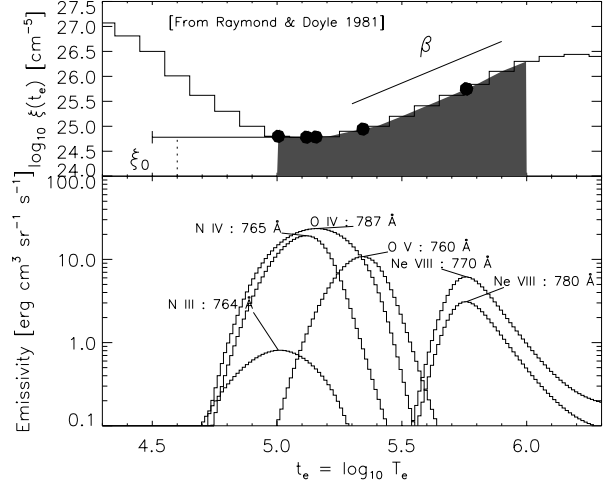


Figure 2. A Graphical depiction of our method is demonstrated. The upper panel shows the DEM curve derived by Raymond & Doyle (1981), the shaded area marking the temperature region of interest ($5 \leq t_e \leq 6$), the loci of the line emissivity maxima τ_i (derived from the lower panel), and guides for the value of β (the gradient in $\log_{10} \xi(t_e)$) and the absolute value, ξ_0 (the intercept of $\xi(t_e)$ at $t_e = 5$).

emission line i we have

$$I_i \approx \int_{\tau_i - 0.3}^{\tau_i + 0.3} K_i(t_e) \xi(t_e) dt_e [\text{erg cm}^{-2} \text{ s}^{-1} \text{ sr}^{-1}] \quad (1)$$

where τ_i is the symbol denoting the temperature at which the emissivity of line i ($K_i(t_e)$) is largest. In order to produce the DEM quadrature we assume that $\xi(t_e)$ does not vary considerably over the range R [$\tau \pm 0.3$]. So, with this assumption in mind we can see, simply, that $\xi(\tau) = I_i / \kappa$ where $\kappa = \int_R K_i(t_e) dt_e$. Therefore, with each line's emissivity peaking at a different temperature (Table 1) we are able to construct the desired DEM grid. Note that the integrated line intensities are determined from GA-Gaussian fits to the line-profiles of the raw data (McIntosh et al. 1998).

Following the production of this DEM grid at *each* spatial and temporal position (x, t) we have to find a way to study its variations. From Jordan (1980); Raymond & Doyle (1981) (and Fig 2), we see that, in the TR temperature region ($5 \leq t_e \leq 6$), $\log_{10} \xi(t_e) (\equiv \Xi(t_e))$ can be approximated by a straight line with gradient β and absolute magnitude (or y-intercept) ξ_0 . We note that the values of β and ξ_0 are proxies of critical components in the energy equation of the solar plasma and particularly the TR; the conductive and the radiative components, respectively, see below. To extract β and ξ_0 we fit a straight-line through the nodes of the grid formed by Eqn. (1), such that

$$\log_{10} \xi(t_e) = \Xi(t_e) = \xi_0 + \beta t_e. \quad (2)$$

Of course, every step of this process is subject to errors in the observations, but we will not explicitly

discuss this here (see McIntosh & Judge 2002), suffice to say that the effect of counting statistics (from the line intensities) on the derivation of ξ_0 and β is small³, see Panel (D) of Fig 3 and below. Thus, for each x and t , we obtain a distribution describing the variation of $\Xi(t_e)$ and an error contribution from variations in the observed line intensities.

In the following section we will interpret the derived values of β and ξ_0 in terms of the energy equation of the TR plasma.

3. INTERPRETATION

The energy flux balance over small temperature bands, like $R = [\tau \pm 0.3]$ above, of the solar transition region (TR), in the absence of flows, can be expressed (following Jordan 1980) as

$$\Delta F_M = \Delta F_R - \Delta F_C, \quad (3)$$

where $\Delta F_M (= \int_R E_{diss} dh)$ is the energy deposited by the as yet unknown (mechanical ?) heating mechanism, ΔF_R is the energy lost by radiation and ΔF_C is the energy lost by conduction. Following Jordan (1980), who assumed vertical magnetic fields, constant pressure, etc (a “classical” TR), we see that these conductive and radiative fluxes can be expressed as

$$\Delta F_M = C_0 \xi_0 T_e^{\beta-1} + \frac{C_1}{\beta+1} T_e^{5/2} - C_2 \frac{3/2-\beta}{\beta+1} T_e^{(3/2-\beta)} T_C^{(\beta+1)} \quad (4)$$

where T_e is the median temperature of the narrow band, T_C is the “coronal temperature” (in this analysis, the temperature of the Ne VIII lines), C_i ($i = 0, 1, 2$) are numerical/physical constants. The first term on the right of Eqn. (4) comes from the radiative flux and the other two from the conductive flux; the dependence of the relative magnitude of these components, and hence ΔF_M , on ξ_0 and β is clear.

Following the procedure outlined in the previous section we are able to produce maps, in space and time, of $\xi(t_e)$ and hence ξ_0 and β . Such maps, for a subset of the available SUMER spatial pixels are provided in Fig. 3 (Panels A and B). The panels on the right of Fig. 3 demonstrate the variability of β only. Panel C shows how a frequency distribution of β values changes from one position to the next, whereas Panel D demonstrates the spatial variation in the $(1 - \sigma)$ variance of these distributions. The smaller vertical bars in Panel D show the contribution to that variance from the Monte-Carlo computation performed on the linear-fits to the DEM grid. In Panel E we show the spatially and temporally averaged distribution of β values, the mean having a value of 1.57 and the variance a value of 0.21; essentially a $\langle \beta \rangle$ of 3/2 as has been found on many occasions before (Mariska 1992). Similarly, there is a corresponding spatially and temporally averaged distribution of ξ_0 with a mean and variance of 6.10^{17} and 3.10^{15} respectively.

³We perform a Monte-Carlo analysis computing 100 representations of $\Xi(t_e)$. Each of these representations is computed by choosing new values of I_i in Eqn. (1) from the interval $[I_i \pm \sqrt{I_i}]$.

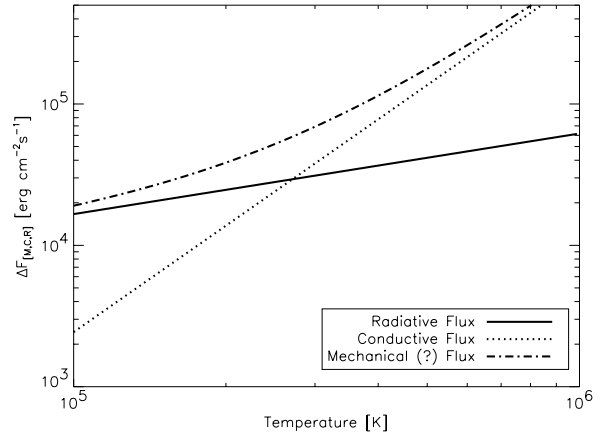


Figure 4. Temperature dependence of the conductive, radiative and mechanical (?) energy fluxes.

What does this mean in terms of the Transition region plasma ? Well, assuming that the spatial and temporal variations in β and ξ_0 are real and not an artifact of the analysis (as might be assumed from the Monte-Carlo derived errors discussed immediately above) we can see, that assuming $\langle \beta \rangle$ of 1.57 and $\langle \xi_0 \rangle$ of 6.10^{17} in Eqn. (4) these terms balance one another at low temperatures, $\sim 2.10^5$ K. However, at the higher temperature end of the region, the conductive term dominates, as one might expect. This is shown in Fig. 4.

4. FUTURE WORK

This very preliminary analysis focuses on the derivation of β and ξ_0 for a series of high resolution SoHO/SUMER and TRACE observations and the implications of these maps for the average structure of the transition region being observed. We have shown that, on average, the region of the solar atmosphere being simultaneously monitored by SoHO and TRACE behaves “classically” in that the gradient of the Differential Emission Measure is 3/2, as had been inferred from previous observations (Skylab, SMM, etc).

In a future paper (McIntosh & Judge 2002) we will discuss the role played in this analysis by the dynamics of the atmosphere; putting aside the “no flows” assumption of Jordan (1980). In addition, we will study the following:

- Variations of $\langle \beta \rangle$ and $\langle \xi_0 \rangle$ by applying various degrees of spatial and temporal binning to the raw data. One obvious conclusion drawn is that, as the spatial and temporal binning of the data is increased the distributions of β and ξ_0 become narrower, but approach a limit, we will investigate that limit.
- The role played by the Ne VIII line pair in “anchoring” the coronal end of the $\xi(t_e)$ computation and their influence on the performing the linear fit to the DEM grid.
- In this brief communication we have only assessed the spatial and temporal averaged behavior of β

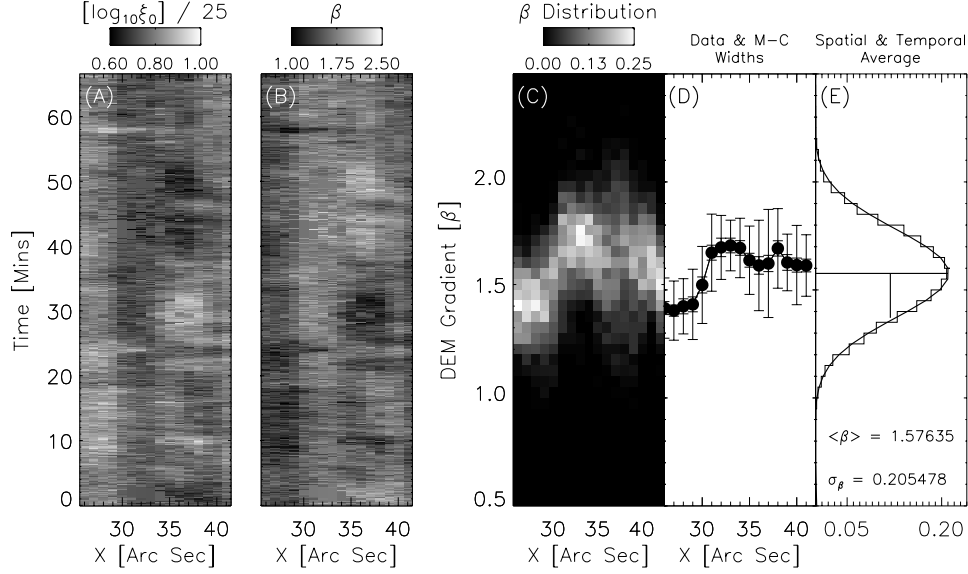


Figure 3. Maps of the absolute value of the DEM ξ_0 (Panel A), the DEM gradient β (Panel B) demonstrate the variability of these components in time and space, and hence the variability of $\xi(t_e)$ in this subset of the available “plage” SUMER pixels. In Panels C & D we show how the histograms of β vary from one spatial pixel to the next. There are two sets of error bars in Panel D, the larger values represents the widths ($1-\sigma$) of the β distributions (they are Gaussian) whilst the smaller values are the contributions to the error at that spatial position from Poisson statistics affecting the computation of β (the Monte-Carlo error estimation technique mentioned in the text). In Panel E we see that the spatial and temporal average of the β distributions is Gaussian and is peaked at 1.58 with a $1-\sigma$ variance of 0.2. Therefore β is effectively $3/2$ on average.

and ξ_0 (and hence F_M , F_R and F_C). We will be able to assess the pixel-to-pixel variation of these quantities and tie them to Doppler velocities of the lines (robustly estimated by the Genetic Algorithm Fits for all the lines analyzed here), extrapolated MDI magnetic fields, visible spatial structures in the TRACE context images (195, 171Å) and simultaneous time-series (1550, 1600, 1700Å) all taken in coordination with SUMER on May 17, 1998. In this way we may be able to observe possible departures from the model of Jordan (1980).

In short, we will address the question: “Once we have model of the plasma temperature structure, through $\xi(t_e)$, what can we reliably infer about the energetics of the TR plasma in the field of view?”

The author acknowledges the invaluable help of Dr. Philip Judge, the support of an ESA External Fellowship at NASA/GSFC, the supplementary support of the SoHO-11 SOC/LOC to attend this meeting and the NCAR/HAO visitor program.

REFERENCES

- Athay, R. G. 1966, ApJ **145**, 784
- Cally, P. S. 1990, ApJ **355**, 693
- Craig, I. J. D. Brown, J. C., 1976, A&A, **49**, 239
- Craig, I. J. D., McClymont A. N., & Underwood, J. H. 1978, A&A **70**, 1
- Fleck, B., Domingo, V., Poland, A. I. 1995, The SOHO mission, Kluwer, Dordrecht.
- Handy, B. N., Acton, L. W., Kankelborg, C. C., Wolfson, C. J., Akin, D. J. et al. 1999, Solar Phys., **187**, 229
- Harrison, R. A., Sawyer, E. C., Carter, M. K., Cruise, A. M. Fludra, A. et al. 1995, Solar Phys., **162**, 233
- Jordan, C. 1980, A&A, **86**, 355
- Judge, P. G., Tarbell, T. D., Wilhelm, K. 2001, ApJ, **554**, 424
- Mariska, J. T. 1992, The Solar Transition Region, Cambridge University Press.
- Mason, H. E. & Monsignori-Fossi, B. C., A&A Rev., **6**, 123
- McIntosh, S. W., Diver, D. A., Judge, P. G., Charbonneau, P., Ireland J. & Brown, J. C. A&A Supp. Ser., **bf 132**, 145
- McIntosh, S. W. & Judge, P. G., In preparation
- Raymond, J. C., Doyle, J. G. 1981, ApJ, **247**, 686
- Rosner, R., Tucker W. H., and Vaiana G. S. 1978, ApJ, **220**, 643
- Wilhelm, K., Curdt, W., Marsch, E., Schühle, U., Lemaire, P. et al. 1995, Solar Phys., **162**, 189